1   **The joint application of metaheuristic algorithm and Bayesian Statistics approach for**

2   **uncertainty and stability assessment of nonlinear Magnetotelluric data**

3   *Mukesh Mukesh, *Kuldeep Sarkar, and Upendra K. Singh

4   Department of Applied Geophysics, IIT(ISM) Dhanbad, Dhanbad-826 004, Jharkhand, India

5   * Corresponding authors: Mukesh Mukesh (mukesh4593@gmail.com) and

6   Kuldeep Sarkar (kuldeepsarkar39@gmail.com)

27 **Abstract**

28 In this paper, we have developed the Matlab code for a weighted hybrid of particle swarm

29 optimization (PSO) and gravitational search algorithm (GSA) known as wPSOGSA, GSA, and

30 PSO algorithms to interpret one-dimensional magnetotelluric (MT) data for some corrupted and

31 non-corrupted synthetic data, as well as two examples of MT field data over different geological

32 terrains: (i) geothermal rich area, Island of Milos, Greece, and (ii) Southern Scotland due to the

33 occurrence of a significantly high electrical conductivity anomaly under crust and upper mantle

34 extending from the Midland Valley across the Southern Uplands into northern England. Even

35 though the fact that many models provide a good fit in a large predefined search space, specific

36 models do not fit well. As a result, we used a Bayesian statistical technique to construct and assess

37 the posterior probability density function (PDF) rather than picking the global model based on the

38 lowest misfit error. This is proceeded by 68.27 % confidence interval for selecting a region where

39 PDF is more prevalent to estimate the mean model which is more accurate and close to the true

40 model. For illustration, correlation matrices show a significant relationship among layer

41 parameters. The findings indicate, the wPSOGSA is less sensitive to model parameters and

42 produces well, more stable and reliable results with the least uncertainty in the model that is

43 compatible with existing borehole samples. Furthermore, the present methods resolve two

44 additional geologically significant layers, one highly conductive (less than 1.0 Ωm) and another

45 resistive (300.0 Ωm) over the Island of Milos, Greece, characterized by alluvium and volcanic

46 deposits, respectively, as corroborated by borehole stratigraphy.

47

48 **Keywords:** Magnetotelluric; Inversion; Uncertainty; wPSOGSA; Posterior; Bayesian.

49

50

51

1.0 Introduction

The magnetotelluric (MT) method is a natural source electromagnetic method that explores various natural resources, namely hydrocarbon, minerals, geothermal prospects, groundwater, metalliferous ores, etc. (Nabighian and Asten, 2002; Simpson and Bahr, 2005). Due to its instability, non-unique solution, and algorithm sensitivity, the MT data interpretation is thought-provoking. Many researchers have attempted and developed various inversion algorithms to interpret, improve the model accuracy, convergence speed, stability and reduce the uncertainty of the solutions (Kirkpatrick, et al., 1983; Constable et al., 1987; Rodi and Mackie, 2001; Li et al., 2018; Zhang et al., 2019; Khishe and Mosavi, 2020). There are mainly two categories of the inversion algorithm: first, the local optimization methods namely Conjugate gradient, Levenberg-Marquardt/Ridge regression, Newton-Gauss, Steepest descent, and Occam inversion, requires good initial guess (Shaw and Srivastava, 2007; Wen et al., 2019; Roy and Kumar, 2021) and another is global optimization techniques (i.e., Ant colony optimization, Genetic algorithm, Particle swarm optimization, Gravitational search algorithm, Simulated annealing, etc.) does not require initial guess. Many researchers have carried out numerous metaheuristic optimization algorithms to invert MT data (Dosso and Oldenburg, 1991; Pérez-Flores and Schultz, 2002; Miecznik et al., 2003; Sen and Stoffa, 2013). These algorithms are inspired by the natural phenomenon include Particle Swarm Optimization (Kennedy and Eberhart, 1995), Genetic Algorithm (Whitley, 1994), Bat algorithm (Yang, 2010a), Differential Evolution (Storn and Price, 1997), biogeographically based Optimization (Simon, 2008), Firefly algorithm (Yang, 2010b), Grey Wolves Optimizer (Mirjalili et al., 2014), Ant Colony (Colorni et al., 1991), Gravitational Search Algorithm (Rashedi et al., 2009).

However, unique characteristics, namely exploration and exploitation, persist in global optimization algorithms. For example, the PSO algorithm has a very high potential for exploitation, which implies that the algorithm performs well in local search but is inferior in exploration (Şenel et al., 2019). This suggests that the algorithm has a limited capacity to estimate

78 the best model in an extensive search range. Because of low exploration characteristics, it gets

79 trapped at the local minima (Mirjalili and Hashim, 2010). So, integrating the two algorithms with

80 opposite characteristics is the best way to solve the exploration and exploitation characteristics,

81 which provide better solutions than the results obtained from an individual algorithm.

82   Here, we utilized wPSOGSA, a new global optimization method that takes into account the

83 algorithm based on natural behavior seen in birds, fish, and insects known as Particle swarm

84 optimization (PSO) and gravity-based Newton's law (with high exploration capability) known as

85 Gravity search algorithm (GSA). Researchers interested in artificial intelligence and developing

86 effective optimization algorithms have been drawn to notable characteristics in such social

87 behavior. The wPSOGSA, PSO, and GSA are used to estimate resistivity distribution of a multi-

88 layered 1D earth model using synthetic (noise free and noisy) data for three and four layers cases

89 taken from Shaw and Srivastava (2007) and Xiong et al. (2018), respectively and field MT

90 sounding data for four and six layers cases taken from Jones and Hutton (1979).and Hutton et al.

91 (1989) respectively.

92   Furthermore, numerous (here 10000) models that fit well are optimized for getting the

93 mean model, which is proceeded by calculating posterior PDF based on Bayesian concepts

94 using all accepted models to find the optimal mean solution with the least uncertainty, as well

95 as a correlation matrix to determine the relationships among the layer parameters. Thus, our

96 analysis suggests that the wPSOGSA algorithm offers a more accurate and trustworthy model

97 with better stability, fast convergent rate and the least uncertainty in the model.

98

99 **2.0 Forward Modelling- Magnetotelluric formulation for 1-D earth**

100 The ability to formulate an effective inversion method requires a thorough understanding of the

101 forward modeling technique for the issue of interest. Factors like frequency range, actual

102 resistivity, and layer thickness are used to create synthetic MT apparent resistivity, $\rho_a(\omega)$ and

103 apparent phase, $\varphi_a(\omega)$ data sets. The electromagnetic impedance (Z) for layered structures is

104   described in terms of an orthogonal horizontal electric field, magnetic field, wavenumber (k),

105   reflection coefficient (R), and exponent factor (τ_f) with angular frequency (ω) as (Ward and

106   Hohmann, 1988):

$$Z = \frac{\mu_0 \omega}{k} = \frac{E_x}{H_y} = -\frac{E_y}{H_x}, \tag{1}$$

107

108   Where, the wavenumber(k) $= \sqrt{-i\mu_0\omega/\rho}$, component of electric field (E_x and E_y) and magnetic

109   field component (H_x and H_y).

110   If displacement currents are not taken into account, Eq. (1) becomes

$$Z = \frac{\mu_0 \omega}{\sqrt{-i\mu_0\omega/\rho}} = \sqrt{i\mu_0\omega\rho} = \sqrt{\mu_0\omega\rho}\, e^{\frac{i\pi}{4}} = \omega \frac{(1 - R\, \tau_f)}{(1 + R\, \tau_f)}, \tag{2}$$

111

112   Noisy impedance is calculated by the following equation

$$Z_{noisy} = Z + Z \times (2 \times rand - 1) \times noise_{percent}, \tag{3}$$

113

114   If the angle between impedance phase with E_x is 45^0, then the resistivity (ρ) in half-space of

115   impedance $Z(\omega)$ and time period (T) can be written as

$$\rho(\omega) = \frac{1}{\mu_0 \omega}\, |Z(\omega)|^2 = \frac{0.2T}{\mu_0} \left|\frac{E_x}{H_y}\right|^2, \tag{4}$$

116

117   Thus, the apparent resistivity and apparent phase are defined (Cagniard, 1953; Ward and

118   Hohmann, 1988) as follows:

119   Apparent resistivity, $\rho_a(\omega) = \frac{1}{\mu_0 \omega}[Z(\omega)Z^*(\omega)], \tag{5}$

120   Apparent phase, $\varphi_a(\omega) = tan^{-1}\left(\frac{img(Z(\omega))}{real(Z(\omega))}\right), \tag{6}$

121   Where the exponent factor, $\tau_f = \exp(-2\gamma h)$, the induction parameter $\gamma = \sqrt{i\omega\mu_0/\rho}$, h is the

122   layer thickness, μ_0 is the magnetic permeability for free space, Z^* is the complex conjugate of

123   impedance, and the *rand* is used for generating random number between 0 and +1.

124

125

126

3.0 Methodology

The methodology that we used for joint modeling of metaheuristic global optimization namely

PSO, GSA, and wPSOGSA in Step-1 and posterior Bayesian probability density function

technique in Step-2 to obtain the global model by utilizing the synthetic and field MT apparent

resistivity and phase curves is depicted in the schematic diagram (Fig. 1), and the steps are

described below:
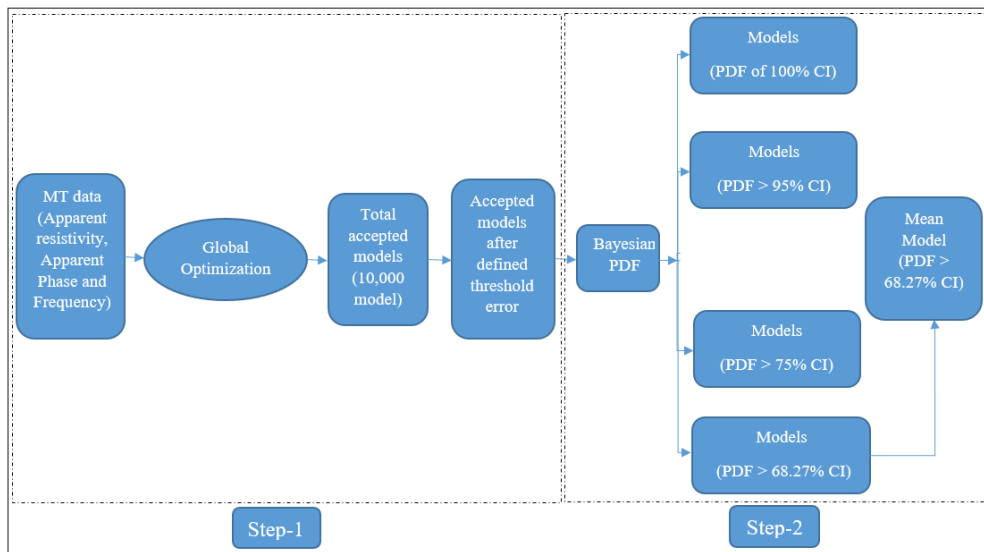
Figure 1 Schematic diagram demonstrating the essential processes considered for joint modeling

of metaheuristic global optimization (Step-1) and posterior PDF technique (Step-2) for obtaining

the global model by utilizing the synthetic and field MT data

3.1 Optimization and Error Estimation

In the present study, we have implemented a new innovative global optimization technique known

as wPSOGSA, in which swarm particles and mass particles provide the best particle, i.e., the best

model. The best model is chosen based on the fitness of the particles, and the cost function or

objective function is used to estimate this fitness. Thus magnetotelluric (MT) inverse problem can

be formulated through the forward modelling operator, *f,* aim at achieving the resistivity model,

144 which illuminates the observed data ρ in the foremost. This operator combines the problem of

145 physics and inverts the observed apparent resistivity data to the resistivity-depth model, *x*, as

146
$$(\rho, \varphi) = f(\boldsymbol{x}) , \qquad (7)$$

147 The cost function (fitness of the particle) is a mathematical relation between observed and

148 calculated data and it is defined as the root mean square error (RMS):

149
$$RMS = \sqrt{\left\{ \frac{(\rho - \rho_C)^2}{N} + \frac{(\varphi - \varphi_C)^2}{N} \right\}} , \qquad (8)$$

150 Where N is the total observed data points, ρ and φ are the observed apparent resistivity and phase,

151 ρ_C and φ_C are the computed apparent resistivity and phase data.

152

153 **3.2 Particle swarm optimization**

154 The particle swarm optimization (PSO) technique is a widespread evolutionary optimization

155 approach for determining the optimal global solution to a nonlinear inverse problem (Kennedy

156 and Eberhart, 1995). This technique is analogous to the particle's natural behavior in search of

157 food with the help of collaborative support from the model population represented by geophysical

158 resistivity solutions/models (known as particles) in a swarming group. The best model/position

159 obtained among the particles so far is stored for each iteration, which helps in search for the best

160 solution, defined by the fitness of each particle estimated using Eq. (8). The particles' velocity and

161 location in the search space are defined for k^{th} particle at t^{th} iteration is given below:

162
$$v_k(t + 1) = w v_k(t) + c_1 \times rand \times \left(x_p - x_k(t) \right) + c_2 \times rand \times \left(x_g - x_k(t) \right), \qquad (9)$$

163
$$x_k(t + 1) = x_k(t) + v_k(t + 1) , \qquad (10)$$

164 where w is the inertia weight set in between 0 and 1, c_1 and c_2 are a personal learning coefficient

165 and a global learning coefficient, respectively, $v_k(t)$ is the velocity of the kth particle at t^{th} iteration,

166 and *rand* is used for a random number between 0 and 1, x_p is the present best solution. x_g is the

167 global best solution, $x_k(t)$ is the position of the kth particle at t^{th} iteration. Particles change their

168   position at each iteration to approach an optimum solution. The first, second, and third terms in

169   Eq. (9) represent exploratory ability, private thought, and particle collaboration, respectively.

170

171   **3.3 Gravitational search algorithm**

172   The gravitational search algorithm (GSA) is a meta-heuristic algorithm based on Newton's

173   gravitational law (Rashedi et al., 2009), which states that mass particles attract each other with a

174   gravitational force that is directly proportional to the product of their masses and inversely

175   proportional to the square of the distance between them. It signifies that massive particles (here,

176   particle represents the resistivity layer model/solution) attract to the neighboring lighter particles.

177   Similar to PSO, the Gravitational search optimizer works with a population of particles known as

178   mass particles in the universe. Thus the best model/solution/particle is achieved among the mass

179   particles. The best model is defined by each particle's capability (i.e., the fitness) calculated using

180   Eq. (8). The initialization of their position in the search spaces is given by

$$x = rand(N, D) \times (up - down) + down \,, \tag{11}$$

182   Where N, D are the number of particles/models, the dimension of the model; and up, and $down$

183   are the upper and lower limit of the search range, respectively.

184   During execution time, the gravitational acting force on agent k^{th} from agent j^{th} at a specific

185   time (t) is defined as

$$F_{k,j}(t) = G(t) \frac{M_{p,k}(t) * M_{a,j}(t)}{R_{k,j}(t) + \epsilon} \left(x_j(t) - x_k(t) \right), \tag{12}$$

187   Where, $M_{a,j}$, and $M_{p,k}$ are the active and passive gravitational masses for particle j and k,

188   respectively, $x_j(t)$ is the position of the particle j at a time t for various parameters, $R_{k,j}$ (t) is

189   Euclidian distance between two particles, and ε is a small constant.

190   Here, gravitational constant $G(t)$ at a specific time t is defined as (Kunche et al., 2015)

191   and acceleration of kth agent at t^{th} iteration for models is $ac_k(t)$ is defined as:

$$ac_k(t) = \frac{F_k(t)}{M_k(t)}, \tag{13}$$

193   Where the gravitational acting force on agent k from agent j and $M_k(t)$ is the mass of the object at

194   a specific time (t).

$$G(t) = G_0 \times \exp\left(-\alpha \times \frac{iter}{maxiter}\right), \qquad (14)$$

196   Where α, G_0, $iter$, and *maxiter* are descending coefficients, starting value of gravitational constant,

197   current iteration, and maximum iterations, respectively.

198   The following equations are used to update the particle's velocity and location:

$$v_k(t+1) = rand \times v_k(t) + ac_k(t), \qquad (15)$$

$$x_k(t+1) = x_k(t) + v_k(t+1), \qquad (16)$$

201   All the particles are randomly placed in the search range using Eq. (11) and then initializes the

202   particle's velocity. Meanwhile, the gravitational constant, total forces and acceleration are

203   computed, and the locations are updated. The end criteria is the misfit error (i.e. 10^{-9}) is taken in

204   our study.

205

3.4 Weighted hybrid PSOGSA (wPSOGSA)

207   The weighted hybrid of PSO and GSA algorithm known as the wPSOGSA algorithm integrates

208   two essential characteristics, exploration (i.e., the ability of an algorithm to search the whole range

209   of a given parameter) and exploitation (i.e., the ability to converge the solution nearest to the best

210   solution) of the global optimization algorithm that increases its efficiency and converges the

211   objective function to achieve global minima. The velocity and location of the particles updated in

212   the wPSOGSA algorithm are illustrated in the schematic diagram (see Fig. 2).

213

214

215

216
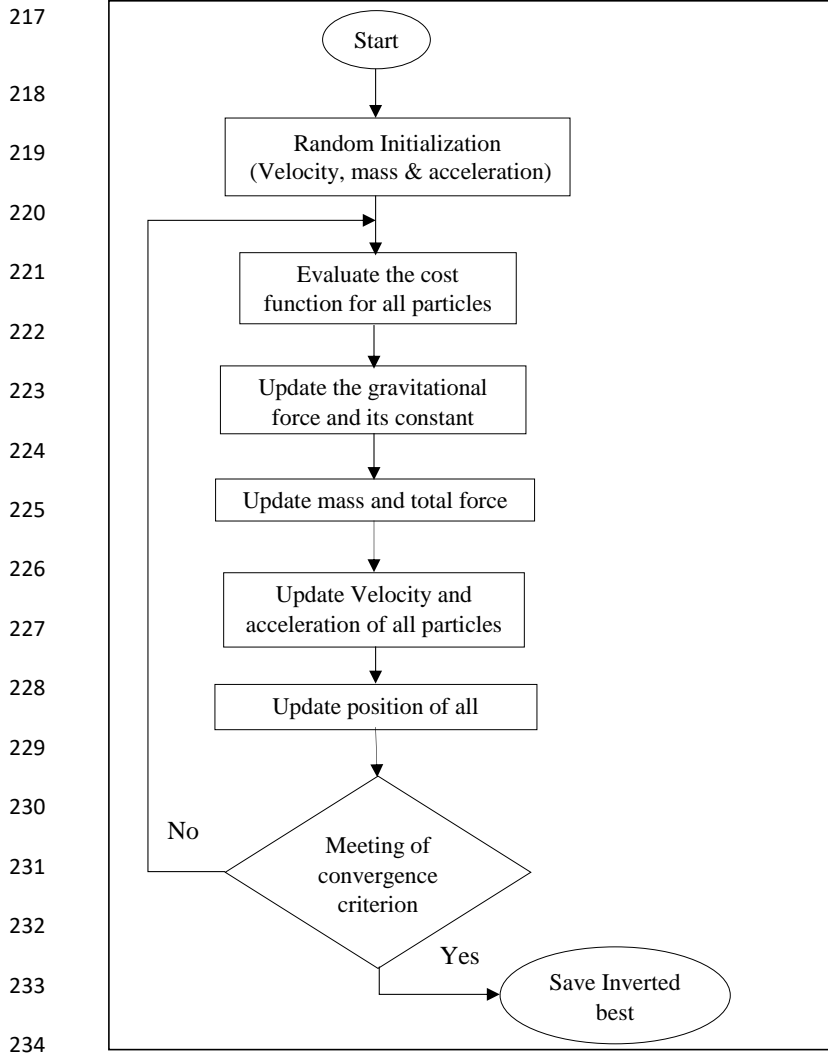
Figure 2 Flow chart of the weighted hybrid Particle Swarm Optimization and Gravity Search

Algorithm known as the wPSOGSA algorithm (After (Mirjalili and Hashim, 2010)

      The wPSOGSA combines the characteristic of social thinking of PSO and the searching

capability of GSA; thus, the particle's velocity is defined as

$$v_k(t+1) = w \times v_k(t) + c_1 \times rand \times ac_k(t) + c_2 \times rand \times (x_g - x_k(t)), \tag{17}$$

Where $v_k(t)$ is the velocity of the particle k at iteration t, w is the weight function (i.e., the constant

which helps to control the momentum of the algorithm to perform optimization properly), ac_k(t)

242   is the acceleration of agent k, x_g is the best solution, and the rand is a random number lies between

243   0 and 1. At each iteration, particles updated their location to achieve the best solution defined as

244   $$x_k(t + 1) = x_k(t) + v_k(t + 1) \,, \tag{18}$$

245   The algorithm starts by randomly initializing the velocity, mass, and acceleration of the

246   particles. The cost function is evaluated for all particles for specified iterations to get the most

247   optimal solution, and inverted results are updated at each iteration. Equation (12), (17), and (18)

248   are used to update the gravitational force, velocity, and location of particles after initialization.

249   However, the velocity and position stop updating their values when the algorithm converge and

250   reaches the least error of the cost function.

251

252   **3.5 Bayesian probability density function**

253   In a Bayesian framework, the probability distribution of the model parameters (known as posterior

254   probability distribution) is computed using given observed data and models obtained from

255   inversion. The posterior for a model is calculated using Bayes' theorem and previous model space

256   information. Individual model parameter ranges are incorporated in the prior knowledge. The two

257   fundamental stages in the Bayesian statistics method are the representation of previous knowledge

258   as a probability density function and calculating the likelihood functional derived from data misfit

259   (Tarantola and Valette, 1982). Specific characteristics, such as the best fitting model, mean model,

260   and correlation matrix may be determined from posterior distribution of models. According to the

261   Bayes' theorem,

262   $$Posterior = prior \times likelihood \,, \tag{19}$$

263   As a result, our priori distribution function for the parameter, x_u, mean priori information, M, and

264   t^2 is the mean uncertainty (μ) is defined as

265   $$f(\mu) = \frac{1}{\sqrt{2\pi t^2}} exp\left\{-\frac{(x_u - M)^2}{2t^2}\right\} \,, \tag{20}$$

266   and likelihood function is

267
$$f(X|\mu) = \prod_{u=1}^{n} \frac{1}{\sqrt{2\pi\sigma^2}} \, exp\left\{-\frac{(x_u-\mu)^2}{2\sigma^2}\right\}, \tag{21}$$

268   Hence the posterior density function calculated for a parameter (x_u) using mean (μ) and variance

269   (σ^2) defined (Lynch, 2007) as

270
$$f(\mu|X) = \frac{1}{\sqrt{t^2\sigma^2}} \, exp\left\{\frac{-(\mu-M)^2}{2t^2} + \frac{\sum_{u=1}^{n}(x_u-\mu)^2}{2\sigma^2}\right\} \tag{22}$$

271   The posterior Bayesian PDF is calculated from accepted models within a set of parameters, as

272   shown below:

273
$$P(X|E) = \frac{P(X)L(E|X)}{\sum_X P(X)L(E|X)}, \tag{23}$$

274   Where, P(X|E) is the posterior probability distribution of the parameter (X) given the evidence

275   (E), P(X) is the prior information of (X) and L(E|X) is the likelihood function of X.

276   After the application of PDF, the study is further proceeded by choosing Confidence

277   Interval (CI) of 68.27 % that is based on the empirical rule, known as the 68-95-99.7 rule (Ross,

278   2009). The model parameters below 68.27 % CI are discarded, and the remaining parameters are

279   used for determining the mean model and uncertainty. Thus, the mean model (P_j) is calculated

280   using the best models having PDF within a 68.27 % CI, defined in the following equation:

281
$$P_j = exp\frac{1}{Nd}\sum ln\left(P_{j,k}\right), \tag{24}$$

282   Here accepted models are used to calculate the correlation matrix (i.e., correlation among

283   model parameters lie between -1 and 1) using the following equation (Tarantola, 2005):

284
$$CovP(l,j) = \frac{1}{Nd}\sum\left(P_{l,k} - P_l\right)\left(P_{j,k} - P_l\right), \tag{25}$$

285   and
$$CorP(l,j) = \frac{CovP(l,j)}{\sqrt{CovP(l,l) \times CovP(j,j)}}, \tag{26}$$

286   Here, *N* is the total number of models, d is used for the number of the layer parameters, $P_{j,k}$ is the

287   j^{th} model parameter of kth model where *l* and *j* both vary from 1 to d (number of layer parameters).

288    $CovP(l,j)$ is the covariance matrix between model parameter *l* and *j*, $P_{l,k}$ is the model parameter

289   lth model parameter of kth model and $CorP(l, j)$ is the correlation matrix between model parameter

290   l and j.

291

4.0 Results and discussions

293   Different MT datasets are utilized to evaluate the proposed wPSOGSA algorithm's effectiveness,

294   sensitivity, stability, and robustness in outlining the genuine subsurface structure. These datasets

295   are noise-free and Gaussian noise synthetic data produced for several geological formations, and

296   two MT field data have been optimized for analysis.

297

4.1 Application to synthetic MT data-Three layers case

299   To demonstrate and evaluate the robustness of the present algorithms, we have generated apparent

300   resistivity and apparent phase synthetic MT data without noise and with noise levels (10 % and

301   20 % noise) considering a three-layer typical continental crustal model with a total thickness of

302   33000 m (i.e., 33.0 km) having a resistivity of middle crust 5000.0 Ωm with 18000 m (i.e., 18.0

303   km) thickness (reasonable low resistive layer) and resistivity of upper-crust 30000.0 Ωm with

304   15000 m (i.e., 15 km) thickness (high resistive layer) underlain by 1000 Ωm (low resistive) half

305   space taken from Shaw & Srivastava (2007).

306   This synthetic MT data that was executed for 10000 runs keeping the same lower and upper

307   bounds as given in Table 1, and iteration to 1000. Figure 3 shows (a) the observed apparent

308   resistivity with the computed data, (b) the observed apparent phase with the computed data, (c)

309   1D inverted model by wPSOGSA (red color), GSA (green color) and PSO (blue color) with a true

310   model (black color), and 2(d) shows the relation between misfit and iterations for the noise-free

311   synthetic data.
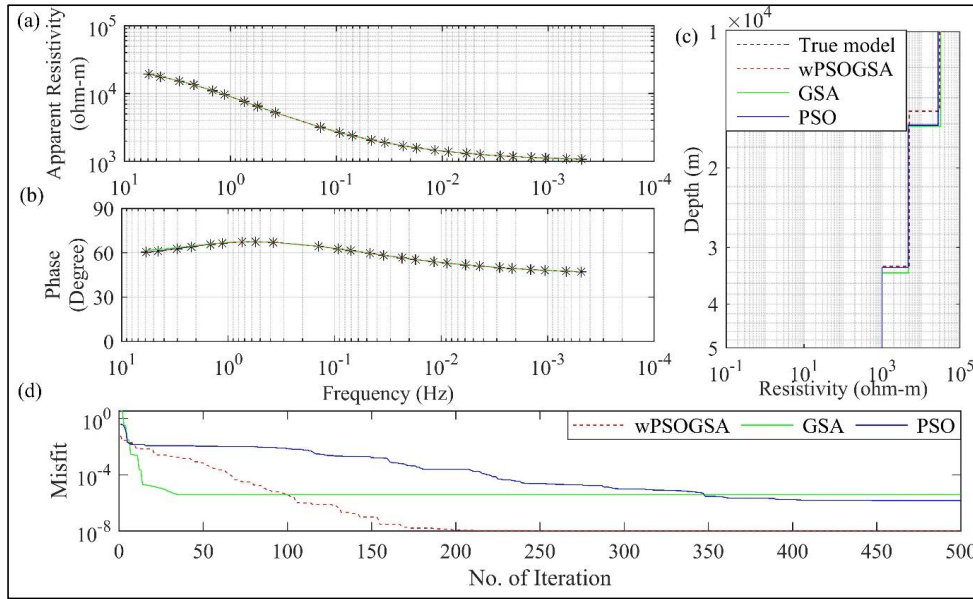
Figure 3 The inverted MT response by PSO (blue color), GSA (green color), and hybrid wPSOGSA (red color) with a true model (black color) over three-layer synthetic data as shown in (a) observed and calculated apparent resistivity curve, (b) observed and calculated apparent phase curve, (c) 1D depth inverted model, and (d) misfit error versus iterations

The misfit curve as shown in Fig. 3(d) is gradually decreasing with increasing iterations and becomes constant, where the algorithm converges. The PSO, GSA, and wPSOGSA converge at iterations 492, 35, and 316 with associated errors 1.51e–6, 3.97e-6, and 1.035e-8, and the associated computational time is 27.06 seconds, 1.75 seconds, and 3.35 seconds, respectively. Thus the curves describes that wPSOGSA converges at the least RMS error. Whereas PSO, GSA, and wPSOGSA using 10 % noisy synthetic data converge at 102, 88, and 358 iterations with an associated error are 0.00435, 0.00439, and 0.00426, and associated computational times are 5.61 seconds, 4.40 seconds, and 3.80 seconds, respectively.

Figure 4 presents the 20 % noisy synthetic MT data that was executed for 10000 runs keeping the same lower and upper bounds, and iteration to 1000. The well fitted inverted MT response (see Fig. 4) as follows: (a) the corrupted synthetic and calculated apparent resistivity

328 data, (b) the corrupted synthetic and calculated apparent phase data, (c) the inverted 1D depth

329 model, and (d) convergence response in terms of misfit error versus iterations. We analyzed Fig.

330 4(d) and found that the PSO, GSA, and wPSOGSA using noisy synthetic data converge at

331 iterations 236, 7, and 73 with associated errors 0.0394, 0.0408, and 0.0393, respectively.

332
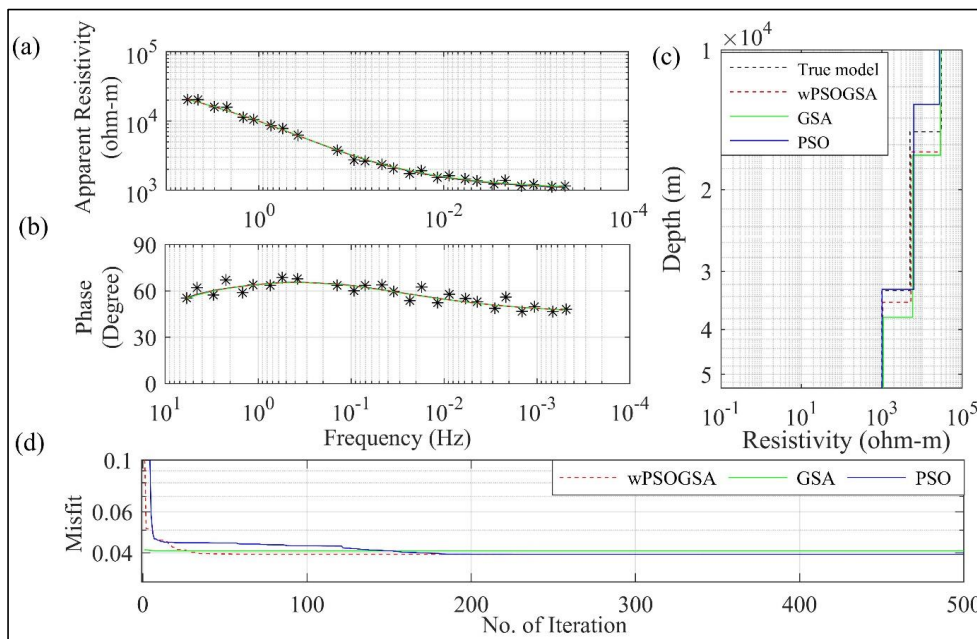
333

334 **Figure 4** The inverted MT response by PSO (blue color), GSA (green color), and hybrid

335 wPSOGSA (red color) with a true model (black color) over three-layer synthetic data with 20 %

336 random noise as shown in (a) observed and calculated apparent resistivity curve, (b) observed and

337 calculated apparent phase curve, (c) 1D depth inverted model, and (d) misfit error versus iterations

338

339 **4.1.1 Bayesian analysis and uncertainty in model parameters**

340 Two methods are used to estimate mean solution and uncertainty: one method is the mean solution

341 for all accepted best-fitted solutions acquired from 10,000 runs for all three global optimization

342 techniques; another method is the model derived from all approved solutions using posterior

343   Bayesian PDF within one standard deviation. To get the global best solutions in our study, we

344   incorporated posterior PDF based on the Bayesian approach to enhance the efficacy of the inverted

345   model and minimize the uncertainty in the model. The process for obtaining the mean solution is

346   proceeded by selecting an initial threshold error which is essential because the smaller the

347   threshold value, the more significant number of models with lesser uncertainty in the model

348   parameters (Sharma, 2012). Thus, a more considerable threshold gives a lesser number of models

349   with enormous uncertainty in the model parameter (Sen and Stoffa, 1996; Sharma, 2012). This is

350   further proceeded by calculating the PDF for each parameter value using Eq. (22). In order to

351   select values of each parameter that having higher posterior PDF, a 68.27 % CI is used. The mean

352   model obtained from selected model parameters is near to the actual model.

353   Figure 5 shows the output of posterior Bayesian PDF, which select model parameters

354   with lesser error. The straight lines (dashed lines) present the actual value of the respective layer

355   parameters. The first layer thickness, second layer thickness, and first layer resistivity have

356   higher uncertainties, i.e., 61.25 m, 51.47 m, and 210.61 Ωm, respectively, whereas the second

357   layer resistivity and third layer resistivity have lower uncertainty, i.e., 17.71 Ωm and 0.03 Ωm,

358   respectively.
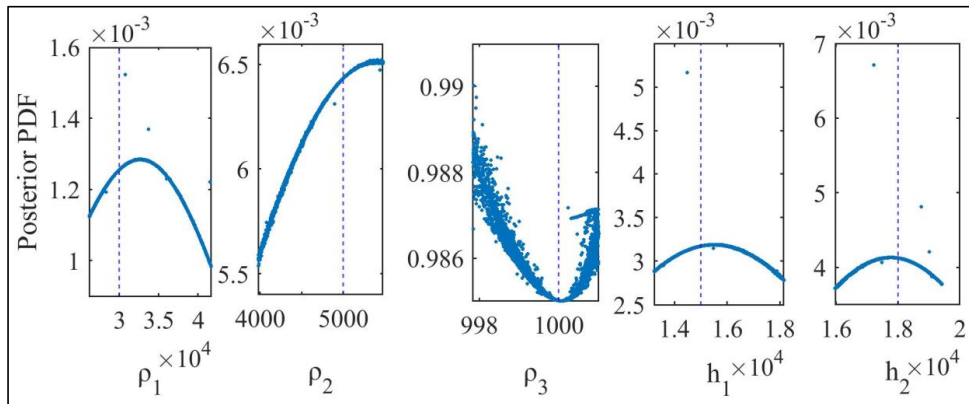
359

360   **Figure 5** Posterior Bayesian probability density function (PDF) with 68.27 % CI for wPSOGSA

361   for three-layered synthetic data

362   **Table 1** True model, search range, and inverted layer parameters by hybrid wPSOGSA, GSA, and

363   PSO for three-layer with different noise (0 %, 10 %, and 20 %) synthetic MT apparent resistivity

364   and apparent phase data.

Layer parameters		ρ_1 (Ωm)	ρ_2 (Ωm)	ρ_3 (Ωm)	h_1 (m)	h_2 (m)
True model		30000	5000	1000	15000	18000
Search Range		5000 - 50000	1000 - 10000	50 - 5000	5000 - 25000	10000- 25000
(Shaw & Srivastava, 2007) 2.0 % Gaussian random noise	PSO	26981.80	6230.30	1011.70	13090	19720
	GA	40800	10000	1010	6210	25000
	RR	43424.40	3097.10	980.70	17010.00	16960.00
0 % noisy data	PSO	27463.86	4664.57	999.48	16112.66	17080.01
	GSA	32017.78	4721.69	1004.05	16195.26	17928.07
	wPSOGSA	30243.42	5007.04	1000.02	14969.33	18029.76
10 % noisy data	PSO	19861.54	7659.73	1022.19	15971.66	14774.31
	GSA	27538.91	6534.61	1018.04	14117.82	17408.14
	wPSOGSA	27589.85	6043.87	998.99	14902.89	18221.87
20 % noisy data	PSO	26981.8	6230.3	1011.7	13090.00	19720.00
	GSA	28823.57	5825.19	1089.65	16861.84	20795.48
	wPSOGSA	29208.75	5282.77	1055.09	16573.22	18398.94

365

366   Table 1 shows the inverted layer parameters using wPSOGSA, GSA, and PSO for noise-

367   free and noisy synthetic MT databased on posterior Bayesian PDF, as well as the actual model and

368   the search range. In addition, layered properties of synthetic data corrupted with 10 % and 20 %

369   random noise are compared and statistically analyzed. Our findings, as shown in Table 1, were

370   compared to those obtained using the Genetic Algorithm (GA), Ridge Regression (RR), and PSO

371   by Shaw & Srivastava (2007), which consistently outperforms GA and RR is closer to the genuine

372   model.
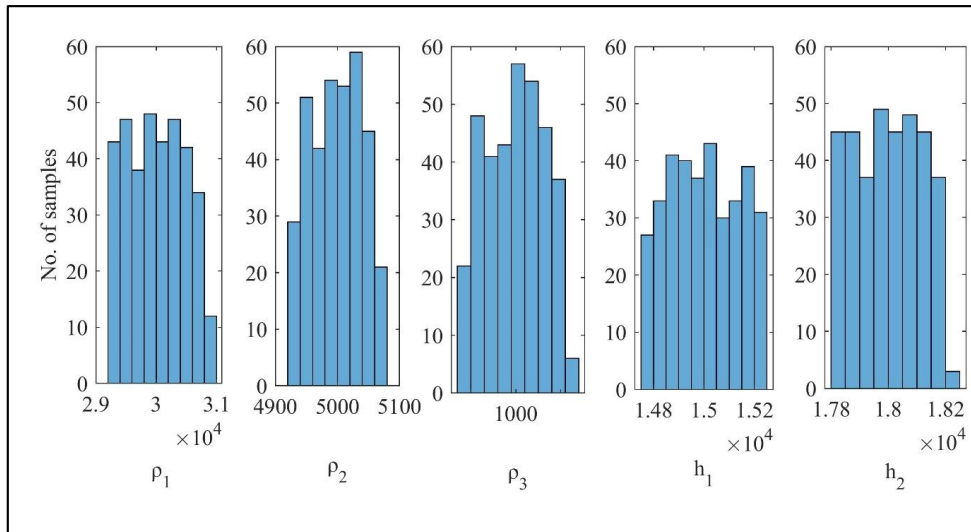
374   **Figure 6** Histogram of selected models for misfit error below a defined threshold error of

375   wPSOGSA

376   Mean value of the accepted model parameters (30243.42 ± 471.26, 5007.04 ± 39.59,

377   1000.02 ± 0.064, 14969.33 ± 136.82, 18029.76 ± 114.90) with high uncertainty of the parameters (1.5

378   %, 0.78 %, 0.0064 %, 0.91 %, and 0.63 %). On the basis of low posterior PDF and high

379   uncertainty, we have taken (ρ_1) and (h_1) for the exercise to show the models are not biased to the

380   selected models.

381   As well as based on the histograms (see Fig. 6), posterior PDF and uncertainty of the

382   inverted layer parameters resistivity (ρ_1) and thickness (h_1) for the three-layered synthetic MT data

383   have been taken to depict the global solution using presented algorithm. Here we prepared the

384   cross-plots of ρ_1 versus h_1 using (a) wPSOGSA, (b) PSO, and (c) GSA, showing all accepted

385   models (red circle), selected models with misfit error less than a threshold error of 10^{-4} (magenta

386   circle), models of a PDF greater than 95 % (blue circle), models of a PDF greater than 75 % (green

387   circle), models of a PDF greater than 68.27 % (yellow circle), and mean model, i.e., model

388   parameters which having a PDF greater than 68.27 % (black asterisk) as shown in Fig. 7. It is

389   noticed that the all inverted results give the global solution which has a good agreement with the

390   true model, whereas wPSOGSA gives the more accurate results than the other two algorithms PSO

391   and GSA as shown in Table 2.

392
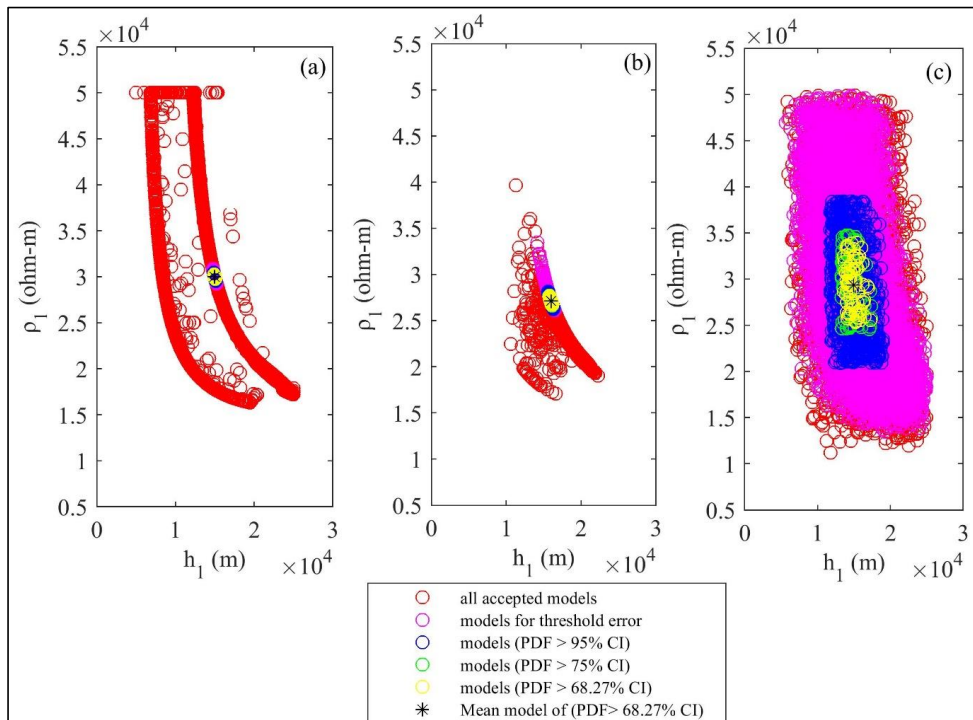
393   **Figure 7** Cross-plots of thickness and resistivity of first layer for the three-layered synthetic

394   resistivity model using (a) wPSOGSA, (b) PSO, and (c) GSA, displaying all accepted models (red

395   circle), selected models with misfit error less than a threshold error (magenta circle), models (pdf

396   > 95 % CI, blue circle), models (pdf > 75 % CI, green circle), models (pdf > 68.27 % CI, yellow

397   circle), and mean model i.e. model parameters which having a PDF greater than 68.27 % (black

398   asterisk)

399

4.1.2 Sensitivity, correlation matrix, and model parameters

The accepted models, which have posterior PDF value within 68.27 % CI, are used to calculate

the correlation matrix. This correlation matrix gives the relationship among model parameters.

Thus, the lesser correlation value gives weak relation among the parameters and vice versa. The

correlation matrix of PSO, GSA, and wPSOGSA was examined on one set of synthetic data, as

shown in Fig. 8, Fig. 9 and Fig. 10, demonstrating the sensitivity among inverted model

parameters. The value of correlation matrix 1.0 indicates that the two parameters are strongly

correlated.

Figure 8 shows that first layer resistivity is correlated highly positively with a first-layer

thickness (0.97) and second layer thickness (0.98), while the second layer resistivity (-0.99) and

third layer resistivity (-0.81) are substantially negative connected. Second layer resistivity is

correlated with the third layer resistivity (0.87) which has a significant positive relationship; while

second layer resistivity has a significant negative correlation with the first layer thickness (-0.99)

and the second layer thickness (-1.00). First layer thickness (-0.92) and second layer thickness (-

0.90) are very negatively associated with third layer resistivity, while first layer thickness is

extremely positively correlated with a second layer thickness (0.99).
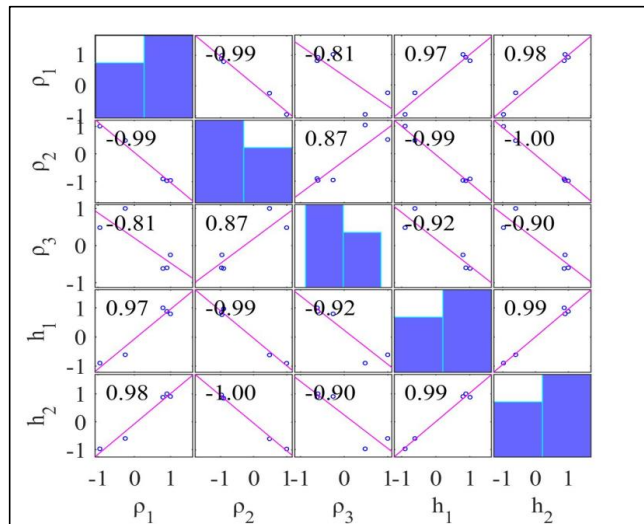
417   **Figure 8** Correlation matrix calculated from PSO inverted model using a three-layer noise-free

418   synthetic MT apparent resistivity and apparent phase data

419

420   Figure 9 indicates that first layer resistivity is highly associated with a second layer

421   thickness (1.00) and weakly with second layer resistivity (-1.00), third layer resistivity (-1.00),

422   and first layer thickness (-1.00). Second layer resistivity (-1) is highly linked with a second layer

423   thickness (-1.00), while third layer resistivity (1.00) and first layer thickness are strongly

424   correlated (1.00). Third layer resistivity has a highly positive correlation with a first-layer

425   thickness (1.00) and a strong negative correlation with a second layer thickness (-1.00), whereas

426   first layer thickness has a significant negative correlation with a second layer thickness (-1.00).
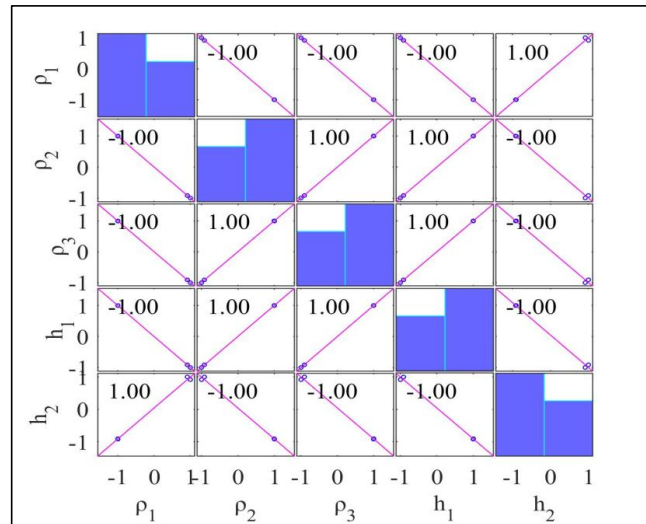
427

428   **Figure 9** Correlation matrix calculated from GSA inverted model using a three-layer noise-free

429   synthetic MT apparent resistivity and apparent phase data

430

431   Figure 10 shows the correlation matrix of wPSOGSA. The analyses reveal that the first

432   layer resistivity is strongly negative with the second layer resistivity, substantially negative (-0.92)

433   with the third layer resistivity, weakly positive (0.30) with the first layer thickness, and

434 considerably (0.63) with the second layer thickness. Second layer resistivity is slightly positive

435 (0.31) when compared to third layer resistivity (0.43) but substantially negative when compared

436 to first layer thickness. Third layer resistivity has a slightly negative correlation (-0.23) with first

437 layer thickness, but a moderately negative correlation (-0.71) with second layer thickness and first

438 layer thickness has a negative correlation (-0.71). Thus the conclusion can be made that the layer

439 parameters are independent of others, so changing one will have no effect on the other compared

440 to the result obtained via PSO and GSA algorithms.
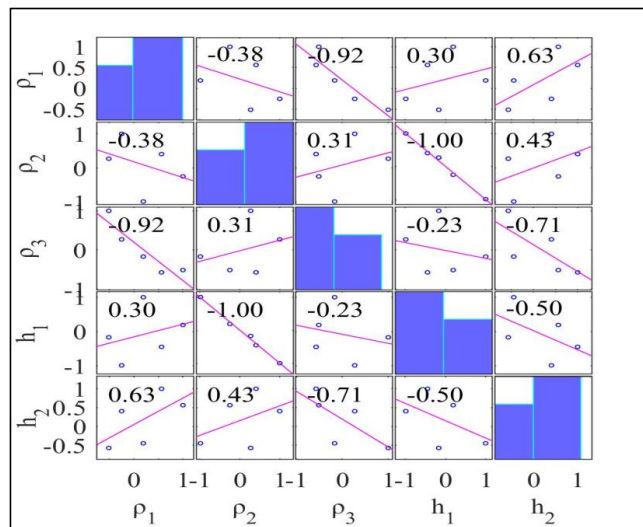
441

442 **Figure 10** Correlation matrix calculated from wPSOGSA inverted model using a three-layer

443 noise-free synthetic MT apparent resistivity and apparent phase data

444

445 **4.1.3 Stability analysis**

446 We used two different search ranges for stability evaluation of proposed wPSOGSA algorithms

447 and executed the algorithms over three layers of synthetic MT data. One of which is expanded,

448 and the other is contracted by 10 % of the initial search range. We infer from three layers of

449 synthetic data, results fluctuate by approximately 3 % from the true value when the search range

450   is changed. This variation is about 10 % on average for synthetic data corrupted with 30 % random

451   noise, as shown in Table 2.

452   **Table 2** Stability analysis of a hybrid algorithm for three layers of synthetic data.

Layer parameters		ρ_1 (Ωm)	ρ_2 (Ωm)	ρ_3 (Ωm)	h_1 (m)	h_2 (m)
Search Range		5000-50000	1000-10000	50-5000	5000-25000	10000-25000
Search Range - Case 1		4500-55000	900-11000	45-5500	4500-27500	9000-27500
wPSOGSA inverted model	0 %	31092.47	5085.79	1000.14	14700.83	18251.85
	30 %	30113.82	5016.75	1137.05	15880.95	23970.22
Search Range - Case 2		5500-45000	1100-9000	55-4500	5500-22500	11000-22500
wPSOGSA inverted model	0 %	29078.26	4922.85	999.91	15273.25	17767.45
	30 %	27815.97	5464.88	1156.46	17398.41	18119.61

453

4.2 Application to synthetic MT data-Four layers case

455   For the second example of the synthetic data, a typical four-layer HK-type of earth model taken

456   from Xiong et al. (2018) is generated by forward modeling equations for demonstration of the

457   wPSOGSA, PSO, and GSA algorithms and compared their performance with Improved

458   Differential Evolution (IDE) results obtained by Xiong et al. (2018). Analysis over noisy synthetic

459   data is done by corrupting synthetic data with 10 % and 20 % Gaussian random noise to mimic

460   the real field data because different types of noises influence apparent resistivity data. Following

461   that, all three optimization methods are run using the noisy synthetic data. As the misfit error

462   increases with the noise in the data, the Bayesian PDF of 68.27 % CI is calculated with respect to

463   the threshold misfit error of 0.01 and thus the mean model is calculated.

464   Enormous uncertainty is shown in the inverted results; hence, we calculated the mean

465   model for 68.27 % CI using posterior Bayesian PDF to reduce the uncertainty and produce the

466   global best solution. The optimized results obtained from the posterior PDF and the true model

467   are shown in Table 3. Fig. 11 illustrate the inverted responses for PSO, GSA, and wPSOGSA are

468   well-fitting as follows (a) observed and calculated apparent resistivity data, (b) observed and

469   calculated apparent phase data, (c) 1-D depth model, and (d) convergence response of present

470   algorithms. We have estimated the layer parameters for synthetic data corrupted with 20 % random

471   noise for comparative analysis and found that the PSO, GSA, and wPSOGSA converge at

472   iterations 96, 556, and 187 with associated errors 3.69, 4.04, and 3.69, respectively.
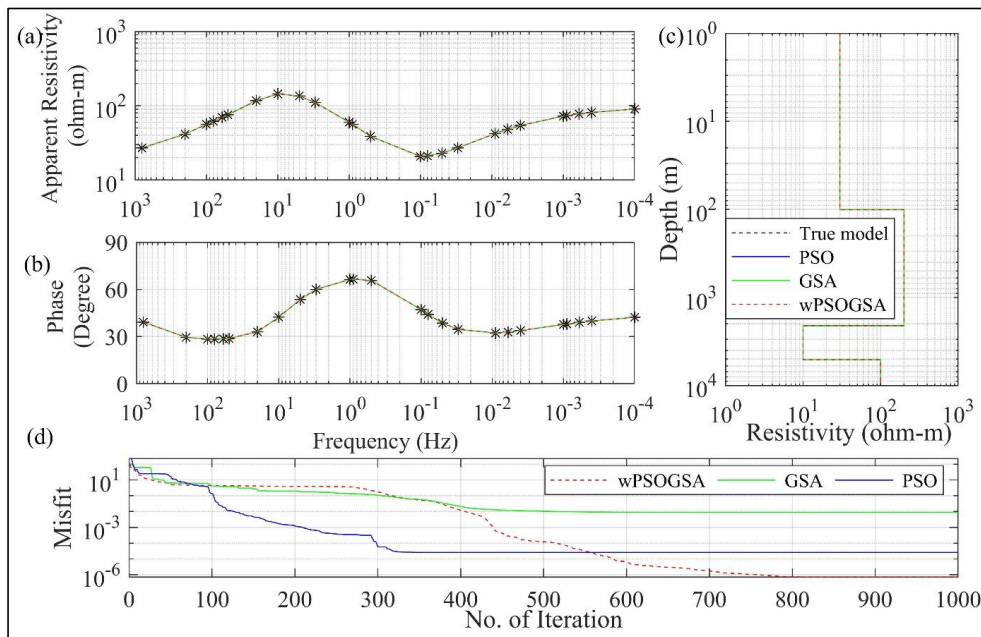
473

474   **Figure 11** The inverted MT response by PSO (blue color), GSA (green color), and hybrid

475   wPSOGSA (red color) with a true model (black color) over four-layer synthetic data as shown in

476   (a) observed and calculated apparent resistivity curve, (b) observed and calculated apparent phase

477   curve, (c) 1D depth inverted model and (d) convergence curve

478   Additionally, the synthetic data corrupted with 10 % random noise is also used and

479   executed inversion, keeping the search range, a number of particles, and iterations the same as

480   before and observed that the PSO, GSA, and wPSOGSA converge at iterations 151, 2 and 250

481   with associated error 1.7609, 1.95 and 1.76 respectively. The posterior Bayesian PDF for threshold

482   data with 68.27 % CI is calculated similarly as a three-layer case to minimize the uncertainty in

483   inverted results.

484

485   **Table 3** Comparison of the result obtained from improved Differential Evolution (IDE) and

486   inverted results of PSO, GSA, and hybrid wPSOGSA obtained by using posterior PDF for four-

487   layer synthetic apparent resistivity data with different Gauss noise levels (0 %, 10 %, and 20 %)

488   and True model.

Layer parameters		ρ_1 (Ωm)	ρ_2 (Ωm)	ρ_3 (Ωm)	ρ_4 (Ωm)	h_1 (m)	h_2 (m)	h_3 (m)
True model		30.00	200.00	10.00	100.00	100.00	2000.00	3000.00
Search Range		25-35	100-250	5-15	50-150	50-200	1000-3000	2000-3500
0 % noise	IDE	30.00	200.00	9.99	100.01	100.00	1991.98	3000.24
	PSO	30.00	200.001	10.00	100.00	100.00	2000.00	3000.00
	GSA	29.95	199.79	9.99	99.99	99.67	2000.70	2995.37
	wPSOGSA	30.00	200.00	10.00	100.00	100.00	2000.00	3000.00
10 % noise	IDE	30.24	210.28	08.92	99.67	109.83	1994.63	2667.13
	PSO	32.86	224.99	11.51	107.65	109.71	1971.78	3499.92
	GSA	29.77	209.78	9.50	106.78	92.38	2073.14	2754.77
	wPSOGSA	30.46	197.18	9.97	102.01	100.50	1974.83	3079.35
20 % noise	IDE	30.30	212.41	11.44	97.92	102.40	1930.17	3347.24
	PSO	34.99	247.04	11.80	114.56	115.16	1986.08	3499.99
	GSA	29.52	225.61	9.74	113.46	87.55	2081.26	2753.29
	wPSOGSA	34.88	246.08	11.75	114.54	114.58	1990.98	3489.10

489

490

4.2.1 Stability analysis

For the stability evaluation of presented algorithms over four layers of synthetic MT data, similar
to the three-layer case, we used two different search ranges and executed the algorithms for 1000
iterations. The method exhibits good results with four layers of synthetic data and reveals minimal
variation for noise-free data. For 30 % contaminated data, the variation is approximately 10 % and
12 % in case 1 and case 2, respectively. The outputs don't change much across runs and provide
consistent results, as shown in Table 4.

Table 4 Stability analysis of a hybrid algorithm for four layers of MT synthetic data.

Layer parameters		ρ_1 (Ωm)	ρ_2 (Ωm)	ρ_3 (Ωm)	ρ_4 (Ωm)	h_1 (m)	h_2 (m)	h_3 (m)
Search Range		25-35	100-250	5-15	50-150	50-200	1000-3000	2000-35000
Search Range-Case 1		27.50-31.50	110-225	5.50-13.50	55-135	55-180	1100-2700	2200-3150
wPSOGSA inverted model	0 %	29.99	199.99	10.00	99.99	99.99	1999.99	3000.00
	30 %	31.5	220.79	11.17	109.18	99.48	2150.07	3150
Search Range-Case 2		22.50-38.50	90-275	4.50-16.50	45-165	45-220	900-3300	1800-3850
wPSOGSA inverted model	0 %	29.99	199.99	10.00	99.99	99.99	1999.99	3000.00
	30 %	35.47	264.27	11.95	103.13	116.22	2020.37	3040.95

4.3 Application to field MT data-Island of Milos, Greece

We utilized the first example of field data from the Island of Milos, Greece. Milos is a part of the
South Aegean Active Volcanic Arc, an example of an emergent volcanic edifice (Stewart and
McPhie, 2006) formed by monogenetic effusive and explosive magmatism pulses. Milos is the
world's biggest exporter of bentonite, and it also has a diverse variety of metalliferous and non-
metalliferous mineral reserves. It's a conserved on-land laboratory for studying shallow

507   underwater hydrothermal ore-forming processes. The accompanying shallow subsurface

508   hydrothermal venting fields have developed significantly less attention. ("Dawes, 1986) used

509   magnetotelluric data to assess the resistivity structure of the geothermal area on Milos west side.

510   With around 3.0 km spacing, 37 MT probes in the bandwidth of 100-0.01 Hz and 12 investigations

511   in the bandwidth of 0.01-0.0001 Hz were installed along with various profiles that were

512   perpendicular to the Zephyria graben in the W-E direction, as well as along the graben in S-N

513   direction (Hutton et al. 1989). The location of the MT site and the geology of the study area are

514   shown in Fig. 12.

515   In one-dimensional MT data for site G5 near borehole M2 (Hutton et al., 1989) the

516   apparent resistivity and phase values are inverted using the wPSOGSA, PSO, and GSA, keeping

517   the same set of controlling parameters as for noisy synthetic data, such as the swarm size, inertia

518   weight (w), personal learning coefficient (c_1) and a global learning coefficient (c_2), descending

519   coefficient (α), and the initial value of universal gravitational constant (G_0).

520   Figure 13 shows the calculated data and model parameters as (a) match between observed

521   and computed apparent resistivity data, (b) match between observed and computed apparent phase

522   data, and (c) 1D inverted model and (d) convergence response of wPSOGSA (red color), GSA

523   (green color), and PSO (blue color) along with true model (black color). In subfigure Fig. 13(c)

524   depicts alluvium deposits with a resistivity of 1.0 Ωm with 15 m thickness as the top layer, and

525   volcanic deposits with a resistivity of 300 Ωm and 10 m thickness lie beneath the alluvium

526   deposits. A very high conducting layer of resistivity less than 1.0 Ωm is estimated, equivalent to

527   the green lahar under the high resistivity volcanic deposits. The next layer below, with higher

528   resistivity, corresponds to the crystalline foundation. In the geothermal zone's depths, the

529   resistivity drops again. The resistivity in the depth range of about 1000 m, which is similar to

530   earlier studies, was explored, and the findings of the proposed algorithm discovered to be in good

531   agreement with model developed by Dawes in Hutton et al. (1989).

532
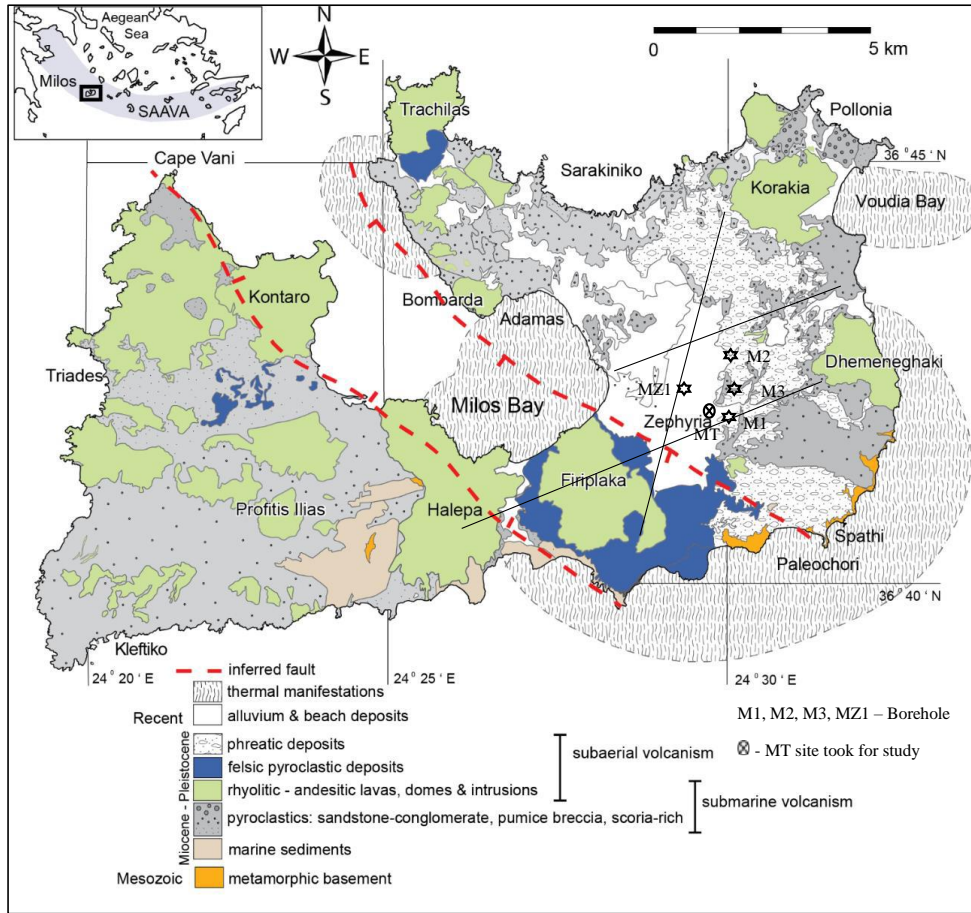
Figure 12 The location of the MT site and geology of the Island of Milos, Greece (modified after (Stewart and McPhie, 2006)

In subfigure Fig. 13(d) reveals that the algorithms converge at iterations 218, 1, and 425 with corresponding errors of 0.0494, 0.0518, and 0.0493 for PSO, GSA, and wPSOGSA, respectively. The hybrid algorithm has the least error between observed and computed data. The algorithms are executed for 1000 iterations and 10000 models, and findings are compared with available stratigraphy, and the result is derived using the Monte-Carlo technique by Hutton et al. (1989). After examining our optimized effects from Fig. 13 and Table 5, hybrid wPSOGSA outperformed PSO and GSA.
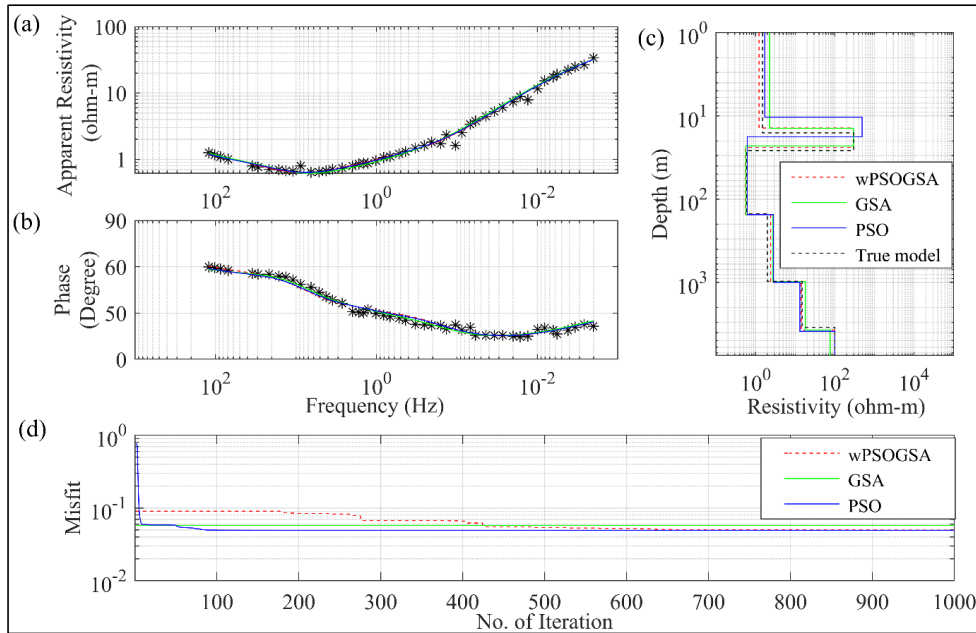
Figure 13 The inverted MT response by PSO (blue color), GSA (green color), and hybrid wPSOGSA (red color) with a true model (black color) over the geothermal area, Island of Milos, Greece, as shown in (a) observed and calculated apparent resistivity curve, (b) observed and calculated apparent phase curve, (c) 1D depth inverted model and (d) convergence curve

4.3.1 Bayesian analysis and uncertainty in model parameters

A posterior Bayesian method determines the global model and related uncertainty. Figure 14 shows another uncertainty study that examined the six-layered resistivity model over the geothermal field, Island of Milos, Greece, and found that the peak values of the posterior PDF for all model parameters are very nearer to the actual value of the layer parameters, providing less uncertainty. We have analyzed the wPSOGSA inverted results from the Fig. 14 and Table 5 and found that the first, second, third, fourth, fifth, and sixth layers' resistivity with uncertainty in associated layer parameters is 1.23±0.49 Ωm, 297.61±53.43 Ωm, 0.55±0.02 Ωm, 2.41±0.16 Ωm, 14.18± 1.76 Ωm, and 99.92±0.37 Ωm. Similarly, the associated thicknesses with uncertainty are

558   14.51±1.35 m, 9.85±1.35 m, 127.39±6.01 m, 823.01±7.57 m, and 2750.88±63.07 m. Thus, the

559   analysis suggests the lesser uncertainties in each layer's parameters except resistivity of the first

560   and second layers.
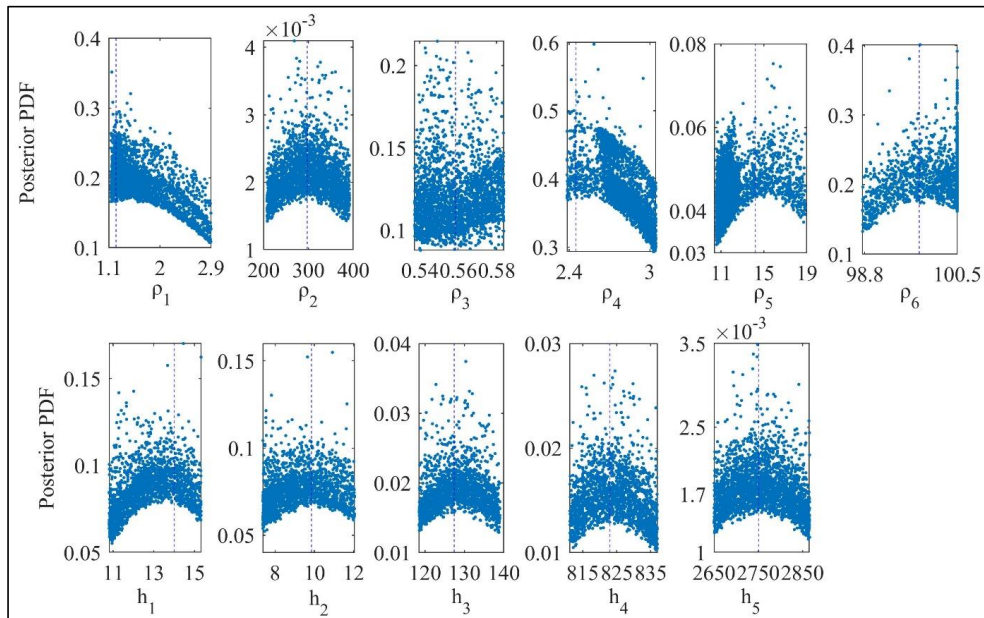
561

562   **Figure 14** Posterior Bayesian probability density function (PDF) with 68.27 % CI for

563   wPSOGSA over a geothermal field, Island of Milos, Greece

564

565   Table 5 compares optimized results obtained from all three presented algorithms based

566   on posterior Bayesian PDF under 68.27 % CI condition. However, the 1D depth model inverted

567   from wPSOGSA shows good agreement with the available borehole M-2 (Hutton et al., 1989).

568   As a result, the hybrid algorithm is functioning better, and the findings are encouraging.

569

570

571

572

573

Table 5 Search range and inverted results by posterior PDF (68.27 % CI) and PSO, GSA, and

hybrid wPSOGSA for six-layered field data.

Layer parameters		ρ_1 (Ωm)	ρ_2 (Ωm)	ρ_3 (Ωm)	ρ_4 (Ωm)	ρ_5 (Ωm)	ρ_6 (Ωm)	h_1 (m)	h_2 (m)	h_3 (m)	h_4 (m)	h_5 (m)
Search Range		0.1-5	50-500	0.1-5	1-10	10-30	50-100	10-20	5-15	110-150	800-850	2500-3000
Mean Posterior	PSO	1.71	493.81	0.62	2.82	13.22	99.97	10.39	7.44	135.4	843.77	2861.35
	GSA	2.28	299.28	0.54	2.76	18.25	76.03	14.08	8.81	130.75	825.32	2753.07
	wPSOGSA	1.23	297.61	0.55	2.41	14.18	99.92	14.51	9.85	127.39	823.01	2750.88

4.3.2 Sensitivity, correlation matrix, and model parameters

Here a similar study of the correlation matrix is carried out for field example from the Island of

Milos, Greece using all accepted models, which have posterior PDF values within 68.27 % CI.

The correlation matrix of PSO, GSA, and wPSOGSA was examined over the field MT data as

shown in Fig. 15, Fig. 16 and Fig. 17 demonstrating the sensitivity among inverted model

parameters and found an almost similar correlation among the layer parameters for three-layer

synthetic study. From correlation analyses, we noticed that the values are showing moderate and

weak correlation among parameters in the wPSOGSA case, indicating that wPSOGSA is linearly

independent of layer parameters, while PSO and GSA are more reliant, so changing one parameter

will show less effect on the other. This indicates that the parameter is less affected by other layer

parameters and resistivity curves. Whereas the correlation among layer parameters for field data

using GSA is either strongly positive or strongly negative, which describes that the parameters are

589 dependent on each other. Thus a change in one parameter affects the other, and also apparent

590 resistivity curve is very much involved.
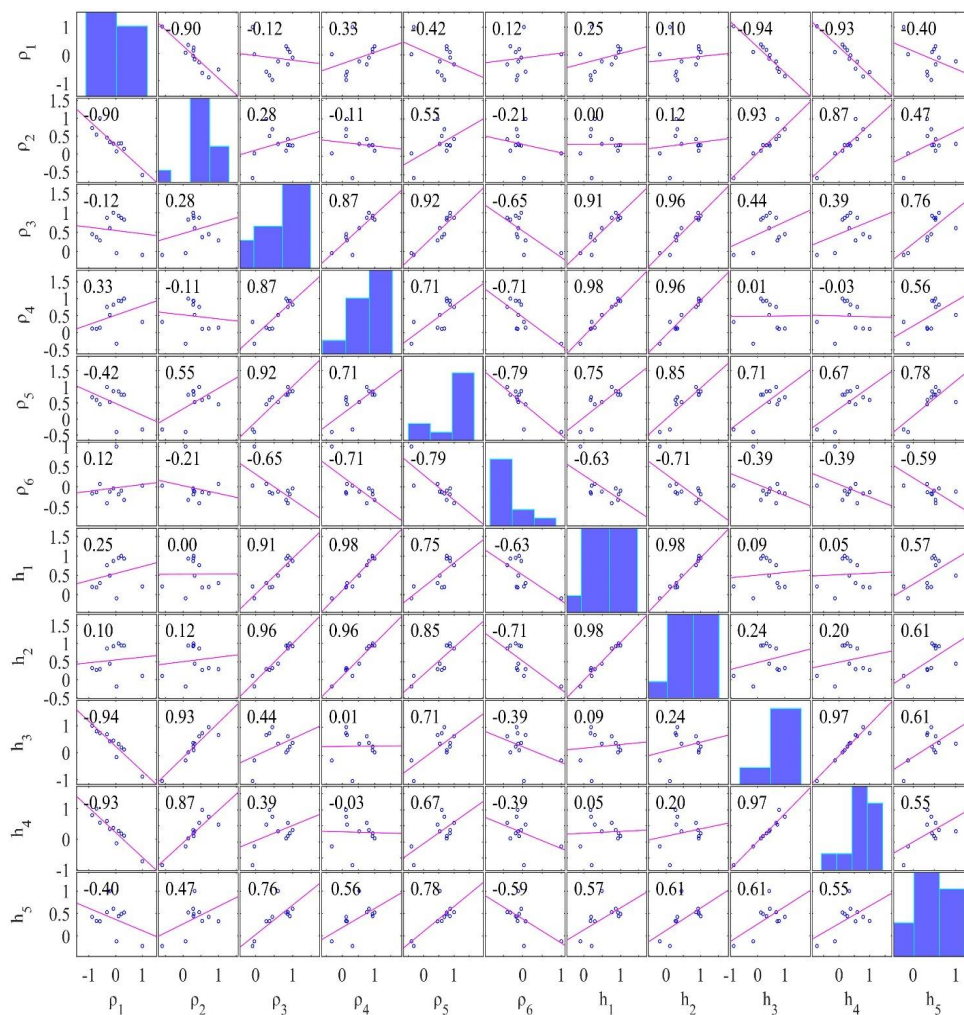
591 **Figure 15** Correlation matrix of field data taken from the geothermal rich area, Island of Milos,

592 Greece for PSO
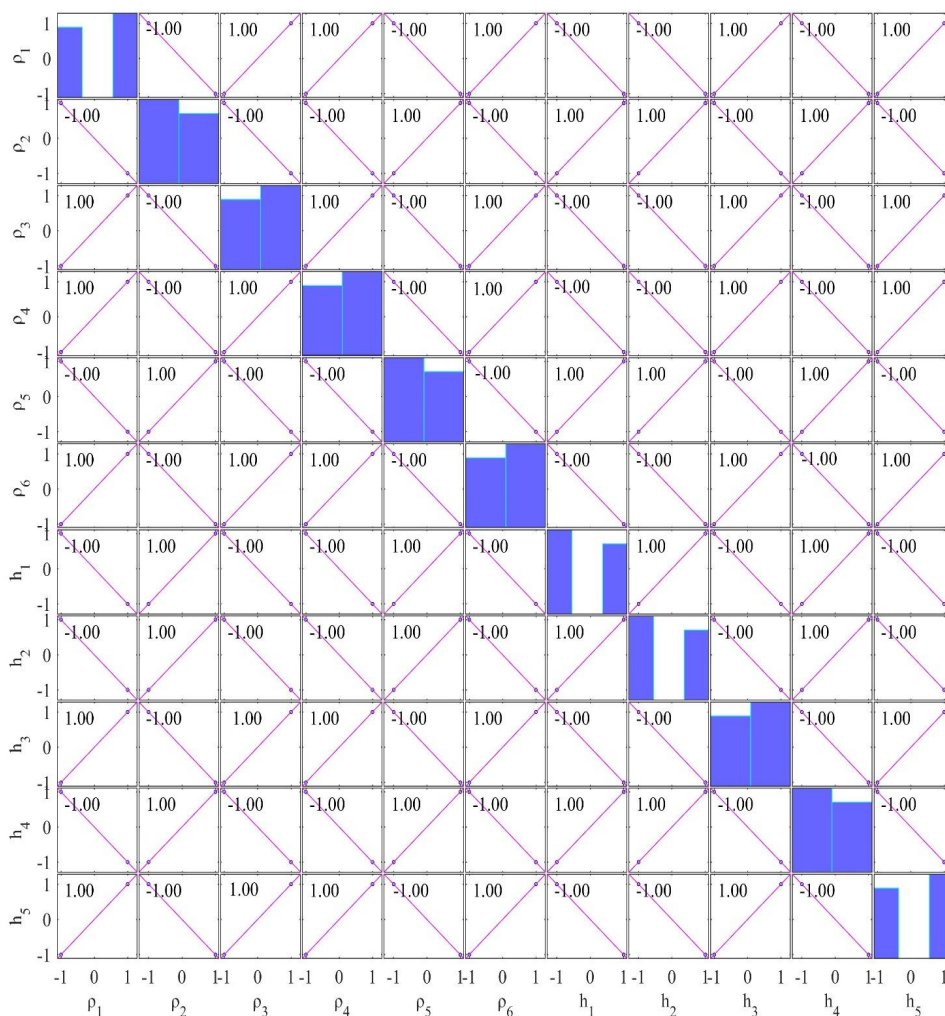
Figure 16 Correlation matrix of field data taken from island geothermal rich area of Milos, Greece

for GSA
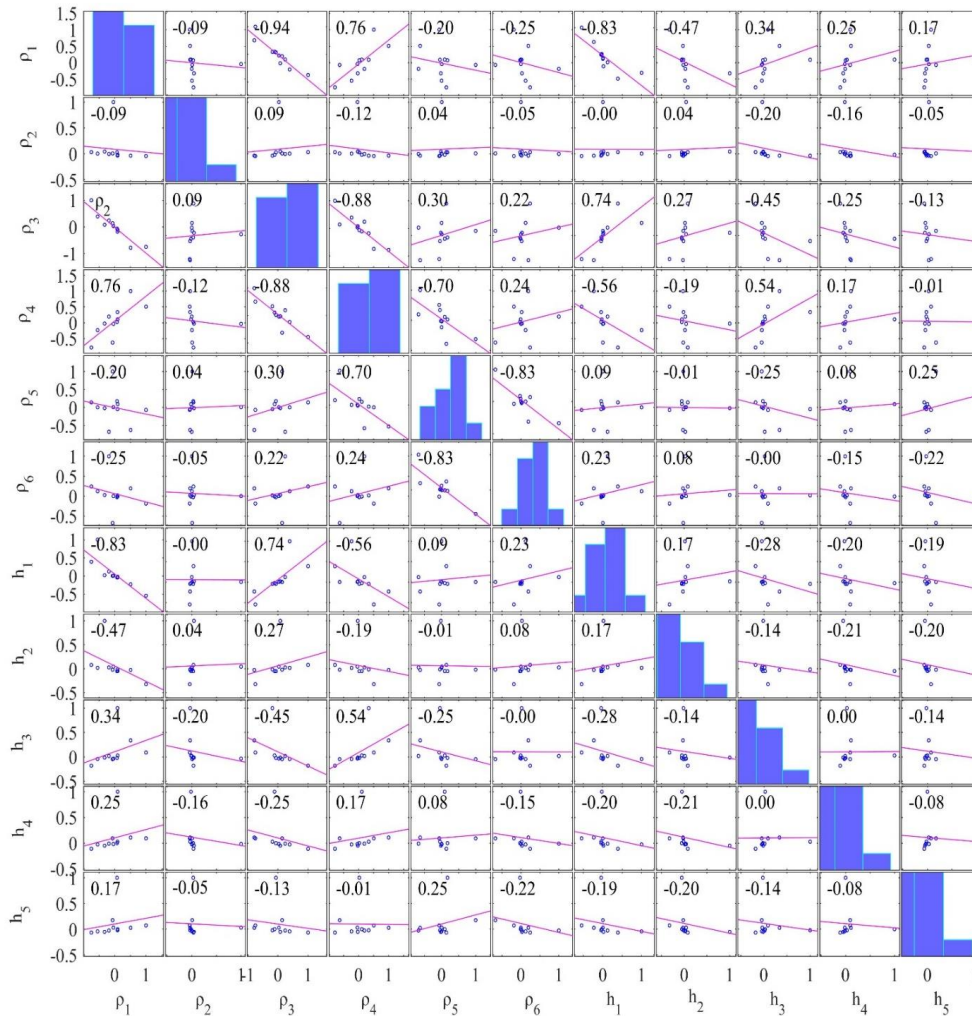
Figure 17 Correlation matrix of field data taken from island geothermal rich area of Milos, Greece

for hybrid wPSOGSA

4.4 Application to field MT data-Newcastleton, Southern upland, Scotland

Another field example of MT data was picked to illustrate our technique from Newcastleton

(2.796° W, 55.196° N in Geographic coordinates), Southern Uplands of Scotland. By the Southern

603 Uplands fault, the Southern Uplands are isolated from the Midland Valley. The bulk of the

604 Southern Uplands comprises Silurian/Lower Paleozoic sedimentary deposits such as greywackes

605 and shales that originated in the Iapetus Ocean during the late Neoproterozoic and early Paleozoic

606 geologic eras. These rocks emerged from the seafloor as an accretionary wedge during the

607 Caledonian orogeny. The majority of the rocks are coarse greywacke, a kind of sandstone that has

608 been poorly metamorphosed and contains angular quartz, feldspar, and small rock fragments. The

609 Midland Valley and Northern England, on the other hand, are known for their thick Carboniferous

610 layers, which are used to measure coal. The geomagnetic studies by Jones and Hutton (1979) have

611 shown that the Southern Uplands are characteristic of a typical continent, with a zone of very high

612 electrical conductivity. The location of the MT site and the geology of the study area are shown

613 in Fig. 18.

614 During nine days in the frequency range of 0.1 Hz to 0.0001 Hz, the variations of the

615 magnetic and telluric fields concerning the time at four sites along a line perpendicular to the

616 anomaly's strike were recorded, keeping a high signal to noise ratio where the anisotropy ratios

617 are so near to one and the skew factor is less than 0.1 for the majority of periods. Due to low

618 anisotropy ratios and skew factor, the resistivity distribution under this location is one-dimensional

619 (Jones and Hutton, 1979). Here one set of MT data is inverted using PSO, GSA, and wPSOGSA

620 to obtain the best fitting apparent resistivity curve, apparent phase curve, and 1D depth model as

621 shown in subfigures Fig. 19(a), Fig. 19(b), and Fig. 19(c), respectively. Figure 19 shows a realistic

622 one-dimensional resistivity variation, with a phase response ranging from 60° at 100 seconds to

623 35° at 1000 seconds, which can only be obtained by establishing a conducting zone at lower

624 crustal/upper mantle levels (Jones and Hutton, 1979).

625 The execution time for wPSOGSA (33 seconds) is the least as compared to GSA (34

626 seconds) and PSO (53 seconds). The convergence iterations are 79, 101, and 65, and associated

627 misfit errors are 3.79, 4.72, and 3.70 for PSO, GSA, and wPSOGSA, respectively.
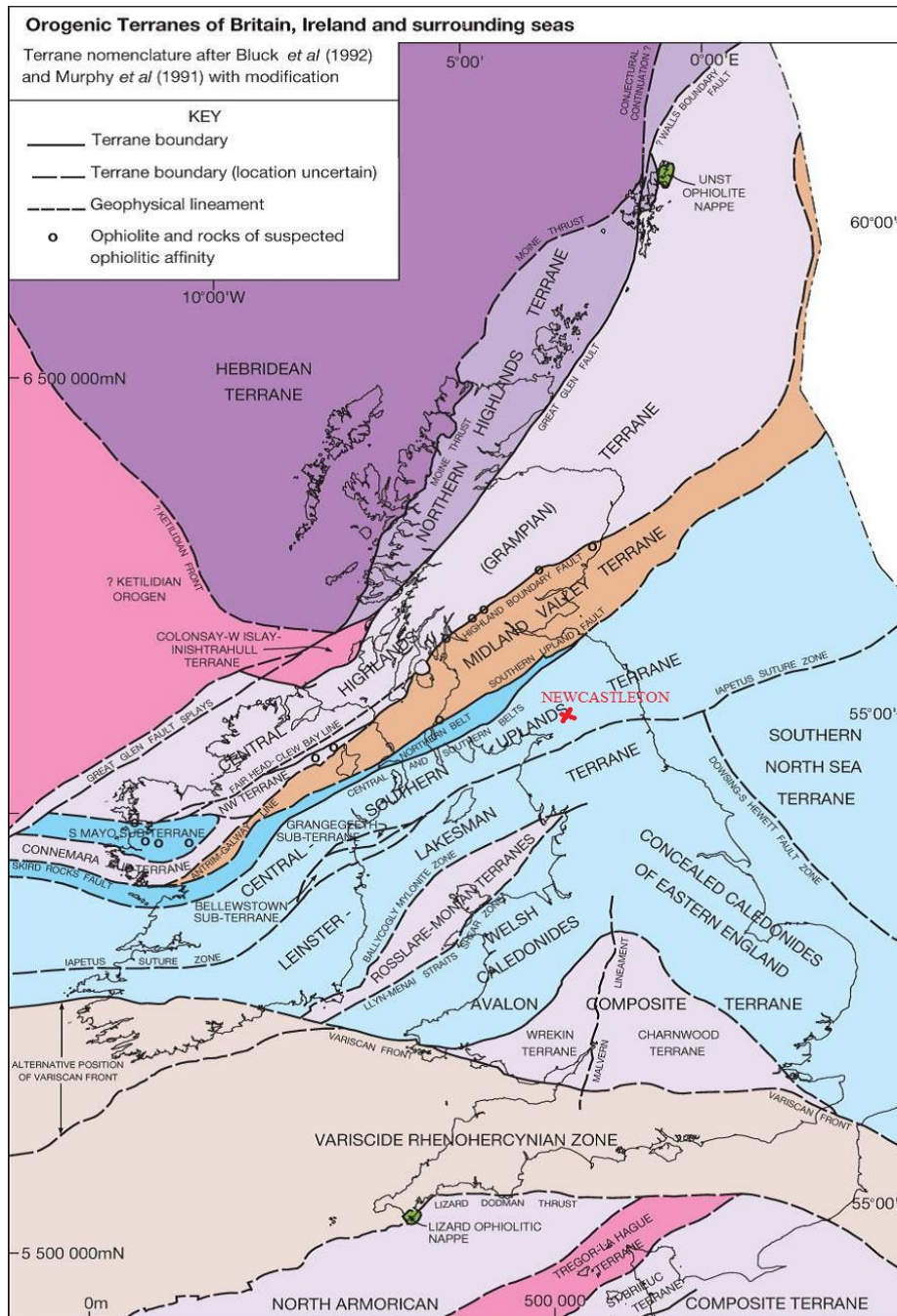
Figure 18 The location of MT site and geology of the Southern upland, Scotland (after BGS, 2016)

631   The inverted MT model is illustrated in subfigure Fig. 19(c), which depicts two low

632   conductive zones at a depth of 21 km and 400 km. The first conductive layer (70 Ωm) with a

633   thickness of 28 km is underlain by a high resistive top layer of thickness of 21 km, and the second

634   very high conductive layer (less than 1.0 Ωm) at a depth of 400 km is underlain by high resistive

635   layer (550 Ωm) of thickness 351 km. Thus the last layer of a very high conductive zone (i.e.,

636   resistivity less than 1.0 Ωm) as a lower crust/upper mantle conductor at a depth of 400 km is

637   estimated. At 400 m depths, a conducting zone meets both the amplitude and phase long period

638   responses. This explanation is directly equivalent to accepted models derived from Monte-Carlo

639   models for the structure underlying the Southern Uplands.
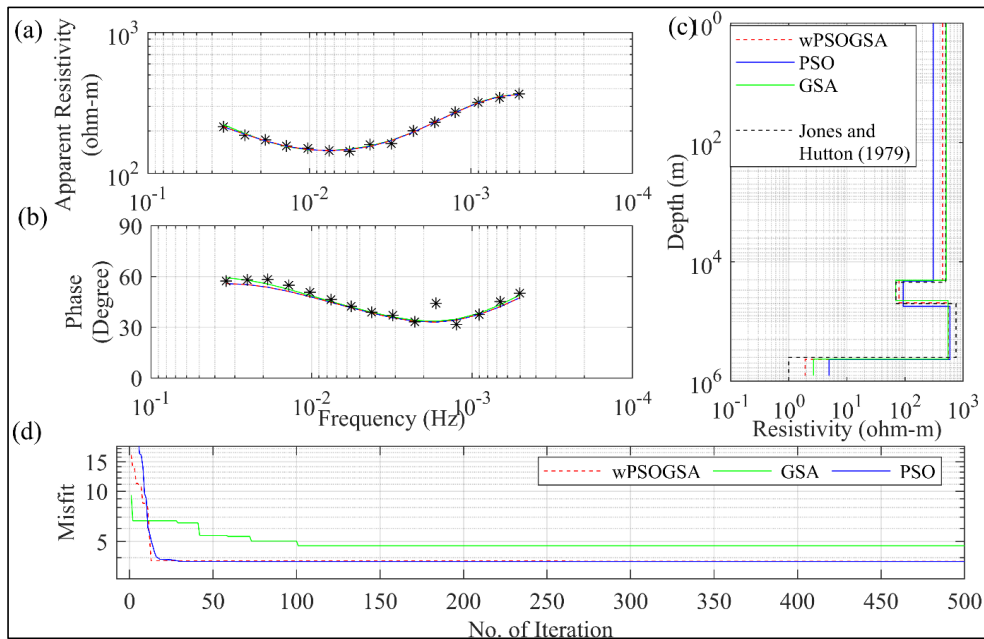
640

641   **Figure 19** The inverted MT response by PSO (blue color), GSA (green color), and hybrid

642   wPSOGSA (red color) with a true model (black color) over Newcastleton, Southern Scotland, as

643   shown in (a) observed and calculated apparent resistivity curve, (b) observed and calculated

644   apparent phase curve, (c) 1D depth inverted model and (d) convergence curve

645

Table 6 Search range, inverted results by posterior PDF (68.27 % CI) using PSO, GSA, and

wPSOGSA for field data.

Layer parameters		ρ_1 (Ωm)	ρ_2 (Ωm)	ρ_3 (Ωm)	ρ_4 (Ωm)	h_1 (m)	h_2 (m)	h_3 (m)
Search Range		300-1000	10-150	250-1500	0.1-5	10000-30000	15000-35000	100000-450000
Mean Posterior	PSO	304.47	92.66	591.52	4.93	20894.01	34776.15	379563.48
	GSA	507.65	69.38	548.46	2.66	20493.18	24182.99	382090.23
	wPSOGSA	444.27	78.94	554.53	1.91	20591.39	28177.40	382181.50

5 Conclusions

The study presented the wPSOGSA algorithm along with PSO and GSA to evaluate their efficacy and applicability to the MT data, which narrates the appraisal of 1D resistivity models from apparent resistivity, apparent phase, and the frequency data sets. So, synthetic and field MT data from various geological terrains were used to demonstrate the relevance of these methods, which are further carried out by applying multiple runs, generating a large number of models that fit the apparent resistivity and apparent phase curves. Then these best-fitting models within a specified range are then chosen for statistical analysis. The statistical analysis includes posterior PDF based on the Bayesian approach with 68.27 % CI, correlation matrix, and stability analysis to enhance the accuracy of the mean model with the least uncertainty. However, a solution from the posterior PDF based on the Bayesian of wPSOGSA is better than GSA, and PSO yields the reliability of the inversion algorithm. In general, conventional techniques can effectively resolve the model in random noise, but they can miscarry in methodical error or inappropriate models. The performance of the proposed algorithms has been analyzed based on the mean model, uncertainty, and stability of layered earth models, and found that the results obtained from wPSOGSA are reliable, stable, and more accurate than the available results, which are fitted well with borehole lithology.

Acknowledgments

666

667 The authors would like to express their gratitude to the IIT(ISM), Dhanbad, for providing a

668 pleasant environment to pursue this study and support for the research. We also express our

669 gratitude to the Editor-in-Chief, Associate Editor, and anonymous reviewers, whose suggestions

670 and comments enabled us to better understanding of the issue and considerably improve our

671 manuscript.

672

673 **Declarations**

674 **Competing interests**

675 The authors have no relevant financial or non-financial interests to disclose and no competing

676 interests to declare that are relevant to the content of this article. All authors certify that they have

677 no affiliations with or involvement in any organization or entity with any financial interest or non-

678 financial interest in the subject matter or materials discussed in this manuscript.

679

680 **Data availability statement**

681 The datasets used for the present study and analysis have been taken from published paper, cited

682 in the manuscript.

683

684 **Authors' contribution statement**

685 **Mukesh:** Conceptualization of the study, Methodology, Computer code, Analysis, Drafting of

686 the manuscript.

687 **Kuldeep Sarkar:** Methodology, Computer code, Analysis, Drafting the manuscript

688 **Upendra K. Singh:** Supervision, Suggestions, and editing.

689

690

691

References

Cagniard, L.: Basic theory of the magneto-telluric method of geophysical prospecting, Geophys, 18, 605–635, https://doi.org/10.1190/1.1437915, 1953.

Colorni, A., Dorigo, M., and Maniezzo, V.: Distributed Optimization by Ant Colonies, Proceedings of the First European Conference on Artificial Life, Paris, France, 134–142 pp., 1991.

Constable, S. C., Parker, R. L., and Constable, C. G.: Occam's inversion: A practical algorithm for generating smooth models from electromagnetic sounding data, Geophys, 52, 289–300, https://doi.org/10.1190/1.1442303, 1987.

"Dawes, G. J. K. ": Magnetotelluric feasibility study: Island of Milos, Greece, Luxembourg, 1986.

Dosso, S. E. and Oldenburg, D. W.: Magnetotelluric appraisal using simulated annealing, Geophys. J. Int., 106, 379–385, https://doi.org/10.1111/j.1365-246X.1991.tb03899.x, 1991.

Hutton, V. R. S., Galanopoulos, D., Dawes, G. J. K., and Pickup, G. E.: A high resolution magnetotelluric survey of the Milos geothermal prospect, Geothermics, 18, 521–532, https://doi.org/10.1016/0375-6505(89)90054-0, 1989.

Jones, A. G. and Hutton, R.: A multi-station magnetotelluric study in southern Scotland – I. Fieldwork, data analysis and results, Geophys. J. Int., 56, 329–349, https://doi.org/10.1111/j.1365-246X.1979.tb00168.x, 1979.

Kennedy, J. and Eberhart, R.: Particle swarm optimization, in: Proceedings of ICNN'95 - International Conference on Neural Networks, 1942–1948 vol.4, https://doi.org/10.1109/ICNN.1995.488968, 1995.

714   Khishe, M. and Mosavi, M. R.: Chimp optimization algorithm, Expert Syst. Appl., 149, 113338,

715   https://doi.org/10.1016/j.eswa.2020.113338, 2020.

716   Kirkpatrick, S., Gelatt C., D., and Vecchi M., P.: Optimization by Simulated Annealing, Science,

717   220, 671–680, https://doi.org/10.1126/science.220.4598.671, 1983.

718   Kunche, P., Sasi Bhushan Rao, G., Reddy, K. V. V. S., and Uma Maheswari, R.: A new

719   approach to dual channel speech enhancement based on hybrid PSOGSA, Int. J. Speech

720   Technol., 18, 45–56, https://doi.org/10.1007/s10772-014-9245-5, 2015.

721   Li, S.-Y., Wang, S.-M., Wang, P.-F., Su, X.-L., Zhang, X.-S., and Dong, Z.-H.: An improved

722   grey wolf optimizer algorithm for the inversion of geoelectrical data, Acta Geophys., 66, 607–

723   621, https://doi.org/10.1007/s11600-018-0148-8, 2018.

724   Lynch, S. M.: Introduction to applied Bayesian statistics and estimation for social scientists,

725   Springer, New York, 2007.

726   Miecznik, J., Wojdyła, M., and Danek, T.: Application of nonlinear methods to inversion of 1D

727   magnetotelluric sounding data based on very fast simulated annealing, Acta Geophys. Pol., Vol.

728   51, nr 3, 307–322, 2003.

729   Mirjalili, S. and Hashim, S. Z. M.: A new hybrid PSOGSA algorithm for function optimization,

730   in: 2010 International Conference on Computer and Information Application, 374–377,

731   https://doi.org/10.1109/ICCIA.2010.6141614, 2010.

732   Mirjalili, S., Mirjalili, S. M., and Lewis, A.: Grey Wolf Optimizer, Adv. Eng. Softw., 69, 46–61,

733   https://doi.org/10.1016/j.advengsoft.2013.12.007, 2014.

734 Nabighian, M. N. and Asten, M. W.: Metalliferous mining geophysics—State of the art in the

735 last decade of the 20th century and the beginning of the new millennium, Geophysics, 67, 964–

736 978, https://doi.org/10.1190/1.1484538, 2002.

737 Pérez-Flores, M. A. and Schultz, A.: Application of 2-D inversion with genetic algorithms to

738 magnetotelluric data from geothermal areas, Earth Planets Space, 54, 607–616,

739 https://doi.org/10.1186/BF03353049, 2002.

740 Rashedi, E., Nezamabadi-pour, H., and Saryazdi, S.: GSA: A Gravitational Search Algorithm,

741 Inf. Sci., 179, 2232–2248, https://doi.org/10.1016/j.ins.2009.03.004, 2009.

742 Rodi, W. and Mackie, R. L.: Nonlinear conjugate gradients algorithm for 2-D magnetotelluric

743 inversion, Geophysics, 66, 174–187, https://doi.org/10.1190/1.1444893, 2001.

744 Ross, S.: Probability and statistics for engineers and scientists, Elsevier, New Delhi, 2009.

745 Roy, A. and Kumar, T. S.: Gravity inversion of 2D fault having variable density contrast using

746 particle swarm optimization, Geophys. Prospect., 69, 1358–1374, https://doi.org/10.1111/1365-

747 2478.13094, 2021.

748 Sen, M. K. and Stoffa, P. L.: Bayesian inference, Gibbs' sampler and uncertainty

749 estimation in geophysical inversion1, Geophys. Prospect., 44, 313–350,

750 https://doi.org/10.1111/j.1365-2478.1996.tb00152.x, 1996.

751 Sen, M. K. and Stoffa, P. L.: Global Optimization Methods in Geophysical Inversion,

752 Cambridge University Press, Cambridge, https://doi.org/10.1017/CBO9780511997570, 2013.

753 Şenel, F. A., Gökçe, F., Yüksel, A. S., and Yiğit, T.: A novel hybrid PSO–GWO algorithm for

754 optimization problems, Eng. Comput., 35, 1359–1373, https://doi.org/10.1007/s00366-018-

755 0668-5, 2019.

756   Sharma, S. P.: VFSARES—a very fast simulated annealing FORTRAN program for

757   interpretation of 1-D DC resistivity sounding data from various electrode arrays, Comput.

758   Geosci., 42, 177–188, https://doi.org/10.1016/j.cageo.2011.08.029, 2012.

759   Shaw, R. and Srivastava, S.: Particle Swarm Optimization: A new tool to invert geophysical

760   data, Geophysics, 72, https://doi.org/10.1190/1.2432481, 2007.

761   Simon, D.: Biogeography-Based Optimization, IEEE Trans. Evol. Comput., 12, 702–713,

762   https://doi.org/10.1109/TEVC.2008.919004, 2008.

763   Simpson, F. and Bahr, K.: Practical Magnetotellurics, Cambridge University Press, 2005.

764   Stewart, A. L. and McPhie, J.: Facies architecture and Late Pliocene – Pleistocene evolution of a

765   felsic volcanic island, Milos, Greece, Bull. Volcanol., 68, 703–726,

766   https://doi.org/10.1007/s00445-005-0045-2, 2006.

767   Storn, R. and Price, K.: Differential Evolution – A Simple and Efficient Heuristic for global

768   Optimization over Continuous Spaces, J. Glob. Optim., 11, 341–359,

769   https://doi.org/10.1023/A:1008202821328, 1997.

770   Tarantola, A.: Inverse Problem Theory and Methods for Model Parameter Estimation,

771   https://doi.org/10.1137/1.9780898717921, 2005.

772   Tarantola, A. and Valette, B.: Generalized nonlinear inverse problems solved using the least

773   squares criterion, Rev. Geophys., 20, 219–232, https://doi.org/10.1029/RG020i002p00219,

774   1982.

775   Ward, S. H. and Hohmann, G. W.: 4. Electromagnetic Theory for Geophysical Applications, in:

776   Electromagnetic Methods in Applied Geophysics: Volume 1, Theory, Society of Exploration

777   Geophysicists, 130–311, https://doi.org/10.1190/1.9781560802631.ch4, 1988.

778   Wen, L., Cheng, J., Li, F., Zhao, J., Shi, Z., and Zhang, H.: Global optimization of controlled

779   source audio-frequency magnetotelluric data with an improved artificial bee colony algorithm, J.

780   Appl. Geophys., 170, 103845, https://doi.org/10.1016/j.jappgeo.2019.103845, 2019.

781   Whitley, D.: A genetic algorithm tutorial, Stat. Comput., 4, 65–85,

782   https://doi.org/10.1007/BF00175354, 1994.

783   Xiong, J., Liu, C., Chen, Y., and Zhang, S.: A non-linear geophysical inversion algorithm for the

784   mt data based on improved differential evolution, Eng. Lett., 26, 161–170, 2018.

785   Yang, X.-S.: A New Metaheuristic Bat-Inspired Algorithm, in: Nature Inspired Cooperative

786   Strategies for Optimization (NICSO 2010), edited by: González, J. R., Pelta, D. A., Cruz, C.,

787   Terrazas, G., and Krasnogor, N., Springer Berlin Heidelberg, Berlin, Heidelberg, 65–74,

788   https://doi.org/10.1007/978-3-642-12538-6_6, 2010a.

789   Yang, X.-S.: Firefly algorithm, stochastic test functions and design optimisation, Int J Bio

790   Inspired Comput, 2, 78–84, https://doi.org/10.48550/arxiv.1003.1409, 2010b.

791   Zhang, Z., Ding, S., and Jia, W.: A hybrid optimization algorithm based on cuckoo search and

792   differential evolution for solving constrained engineering problems, Eng. Appl. Artif. Intell., 85,

793   254–268, https://doi.org/10.1016/j.engappai.2019.06.017, 2019.

794